1 **Processes influencing formation of low-salinity high-biomass lenses near**

2 **the edge of the Ross Ice Shelf**

3

4 Yizhen Li[1], Dennis J. McGillicuddy Jr. [1], Michael S. Dinniman[2], and John M. Klinck[2]

5 [1]Department of Applied Ocean Physics and Engineering, Woods Hole Oceanographic Institution,

6 Woods Hole, MA 02543

7 [2]Center for Coastal Physical Oceanography, Old Dominion University, Norfolk, Virginia 23529,

8 USA

9 Correspondence: Yizhen Li, Phone: 508-289-2238, Email: yzli@whoi.edu

10

11 **Abstract**

12 Both remotely sensed and *in situ* observations in austral summer of early 2012 in the Ross Sea

13 suggest the presence of cold, low-salinity, and high-biomass eddies along the edge of the Ross Ice

14 Shelf (RIS). Satellite measurements include sea surface temperature and ocean color, and

15 shipboard data sets include hydrographic profiles, towed instrumentation, and underway acoustic

16 Doppler current profilers. Idealized model simulations are utilized to examine the processes

17 responsible for ice shelf eddy formation. 3-D model simulations produce similar cold and fresh

18 eddies, although the simulated vertical lenses are quantitatively thinner than observed. Model

19 sensitivity tests show that both basal melting underneath the ice shelf and irregularity of the ice

20 shelf edge facilitate generation of cold and fresh eddies. 2-D model simulations further suggest

21 that both basal melting and downwelling-favorable winds play crucial roles in forming a thick

22 layer of low-salinity water observed along the edge of the RIS. These properties may have been

23 entrained into the observed eddies, whereas that entrainment process was not captured in the

24 specific eddy formation events studied in our 3-D model—which may explain the discrepancy

25 between the simulated and observed eddies, at least in part. Additional sensitivity experiments

26 imply that uncertainties associated with background stratification and wind stress may also

27 explain why the model underestimates the thickness of the low-salinity lens in the eddy interiors.

28 Our study highlights the importance of incorporating accurate wind forcing, basal melting, and

29 ice shelf irregularity for simulating eddy formation near the RIS edge. The processes responsible

30   for generating the high phytoplankton biomass inside these eddies remain to be elucidated.

31   **Key words:** eddies, instability, basal melting, mixed layer processes, ice shelf geometry

32

1. Introduction

The Ross Ice Shelf (RIS) is the largest ice shelf (~4.7×10^5 km^2) in Antarctica, located in the southern Ross Sea (Fig. 1). The RIS region plays host to a number of important physical and biological processes. Air-sea interaction and ice dynamics at the edge of the RIS influence High Salinity Shelf Water (HSSW) formation (MacAyeal, 1984; Orsi and Wiederwohl, 2009), which is a dense water mass that is critical in Antarctic Bottom Water formation (Jacobs et al., 1996; Orsi et al., 2002; Whitworth and Orsi, 2006; Gordon et al., 2009). The frontal region also bridges heat and mass exchanges with the open ocean (Rignot et al., 2013; Depoorter et al., 2013). The Ross Sea is one of the most biologically productive areas in the Southern Ocean (Comiso et al., 1993; Arrigo et al., 1998; Smith et al., 2014), and the RIS delimits the southern boundary of the region of high productivity. Iron supply is thought to regulate primary production in the Ross Sea (Arrigo, 2003; Martin et al., 1990; Sedwick et al., 2000). Although recent evidence suggests that the iron supply from glacial ice melt constitutes only a small fraction of the iron supply to this region (McGillicuddy et al., 2015), basal melting is a primary pathway for iron supply in other Antarctic polynyas (Arrigo et al., 2015; Gerringa et al., 2012).

Processes at different depth levels make the cavity underneath the RIS a complex ocean environment. Near the ice shelf front, increased melting is facilitated by occasional warm water intrusions (Jenkins and Doake, 1991) from adjacent upper ocean waters that come in contact with the edge of the ice shelf. At mid depth, melting is caused by intrusion of modified circumpolar deep water (Jacobs et al., 2011, Dinniman et al., 2007, 2012; Klinck and Dinniman, 2010; Pritchard et al., 2012). In the deepest layer, dense HSSW (a product of brine rejection over the continental shelf from ice formation during the winter months), which is at the surface freezing point, can penetrate into the cavity, causing melting near the grounding line due to the depression of the freezing point of seawater with increasing pressure. As the buoyant meltwaters rise along the ice shelf base, they can re-freeze at mid-depth due to the increase in freezing point with decreasing pressure, producing super-cooled Ice Shelf Water (ISW). All these processes interact with each

61 other at various spatial and temporal scales, making for a complex regime of

62 thermohaline circulation (MacAyeal, 1984; 1985).

63   Of particular interest from the ecosystem perspective is the penetration of glacial

64 meltwater into the surface waters in the interior of the Ross Sea, as this constitutes a

65 source of iron to upper ocean phytoplankton populations. Although the iron supply from

66 glacial meltwater is thought to be small relative to other sources in the Ross Sea

67 (McGillicuddy et al., 2015), physical processes such as oceanic eddies that affect the

68 glacial meltwater may be locally important to the initiation and spatial distribution of

69 regional phytoplankton blooms. In austral summer of 2012, we observed two anticyclonic

70 eddies emanating from the edge of the RIS northward into the Ross Sea. The eddies

71 contained low-salinity lenses with deep mixed layers (ca. 80 m) and very high biomass of

72 the colonial prymnesiophyte *Phaeocystis antarctica* (Smith et al., submitted). Our goal is

73 to identify the processes that lead to generation of these eddy features, which will set the

74 stage for future study of the physical-biological interactions leading to the high biomass

75 observed in their interiors.

76   The primary surface circulation feature along the front of the RIS in this area is a

77 relatively strong, narrow, and fresh coastal current that flows to the west (Jacobs et al.,

78 1970; Keys et al., 1990). A similar westward current is found along the front of the

79 Ronne-Filchner Ice Shelf (Makinson et al., 2006) where mooring observations at depth

80 (as deep as 200-400 m) also suggest the possibility of eddy-driven variability (Nicholls et

81 al., 2003). Knowledge of ocean variability in the near-surface ocean layer near the RIS

82 remains rather limited due the scarcity of data, with relatively few direct observations

83 available (Jacobs et al., 1985; Smethie and Jacobs, 2005). Arzeno et al. (2014) postulated

84 eddies as being responsible for variability in currents underneath the RIS that was

85 uncorrelated with the wind. Although the process of eddy generation has been examined

86 in many oceanic regimes, relatively few studies have focused on instabilities associated

87 with ice-ocean interactions (Clarke et al., 1978; Chu, 1987; Dumont et al., 2010;

88   Häkkinen, 1986; Niebauer, 1982). In general, glacial meltwater can create horizontal

89   density gradients that force a baroclinic jet (Niebauer, 1982). Häkkinen (1986) found that

90   when across- and along-ice edge spatial scales are similar enough, such baroclinic jets

91   can generate eddy structures along the ice edge, especially when the wind forcing is

92   time-varying between upwelling and downwelling conditions. In a modeling study in

93   Baffin Bay near Greenland, cyclonic eddies were generated at the edge of landfast ice in

94   response to frequent northerly wind forcing (Dumont et al., 2010). All of these studies

95   pointed to the importance of baroclinic jets and wind forcing in forming eddies near the

96   ice edge.

97   Earlier efforts utilized idealized two-layer ocean models to study how ice-ocean

98   interactions can excite unstable wave forms. Using a semi-analytical quasi-geostrophic

99   model, Clark et al. (1978) showed that fluctuations in the flow along fast ice can be

100 described as wind-forced trapped long-waves propagating along the ice edge. Chu (1987)

101 used a similar framework, identifying an air-sea interaction feedback mechanism that

102 excites an unstable mode in the presence of curvature in the ice edge. Both Clark (1978)

103 and Chu (1987) highlighted the importance of considering multiple factors such as ice

104 shelf edge irregularity and background stratification (initial conditions) in studying the

105 instability processes. However, because their models did not consider basal melting, they

106 were not able to capture the structure of low salinity features near the ice edge.

107   Our approach is to use high-resolution models with varying levels of complexity to

108 understand the mesoscale phenomena we observed at the edge of the RIS. In section 2 we

109 present the observations, consisting of both satellite imagery and *in situ* measurements.

110 We describe the model configuration in section 3, followed by sections 4 and 5 showing

111 its implementation in three- and two-dimensional configurations respectively. The former

112 is used to investigate the process responsible for eddy generation, whereas the latter

113 provides insight into the mechanisms responsible for the thickness of the low-salinity

114 surface layer. Section 6 offers further analysis and discussion of the dynamics via

115 sensitivity analyses. A summary and conclusions are presented in section 7.

116

117 **2. Observations**

118

119 2.1 Satellite imagery

120   A sequence of satellite images in January 2012 captured the signature and evolution

121 of several eddies near the RIS. On January 22, there were a number of cold eddies along

122 the edge of the ice shelf (Fig. 2a), including some that were already separated from the

123 RIS (e.g., near 177.5°E), and some that remained connected to the ice shelf edge (e.g.,

124 Eddy 1 and Eddy 2). Eddy 1 (radius ~12 km) was flanked by warm anomalies to the east

125 and northwest. Eddy 2 was slightly smaller (radius ~8 km), separated from Eddy 1 by a

126 warm filament protruding south to the edge of the RIS. Satellite ocean color imagery

127 indicated a ca. 20 km wide strip of low chlorophyll *a* (Chl-a) concentrations extending

128 along the edge of the RIS, with much higher concentrations to the north (Fig. 2b). The

129 signatures of Eddies 1 and 2 in ocean color are barely discernible in the January 22 image

130 as northward perturbations to the frontal boundary separating high and low Chl-a.

131   Three days later, the two eddies had moved away from the RIS and evolved in the

132 process (Fig. 3). Both eddies appear to be warmer, and have similar radii that are still

133 larger than the local Rossby deformation radius (~5 km). Eddy 1 moved north-northwest,

134 whereas Eddy 2 moved northwest, narrowing the gap in between them. Both eddies

135 propagated westward, as is commonly the case due to meridional variation in the Coriolis

136 parameter (Cushman-Roisin et al., 1990), although the background westward flow in this

137 region may play a crucial role. Compared to three days prior, Eddy 1 took on a more

138 circular shape. By January 25, Eddy 1 had almost completely separated from the RIS,

139 connected to the shelf edge by only narrow cold filaments running southwest from the

140 southern flank of the eddy and south from the eastern flank of the eddy (Fig. 3a). The

141 warm anomaly previously to the east of Eddy 1 on January 22 appeared to have been

142 swept southwestward by January 25. However, this movement is opposite in direction to

143   that caused by the eddy's counterclockwise rotation (see shipboard velocity observations

144   described in the following section), so if this interpretation is correct then translation of

145   the warm anomaly must have been caused by flow external to the eddy. On January 25,

146   Eddy 2 was still in the process of separation from the ice shelf, with a cold filament

147   linking its southern flank to the cold-water band adjacent to the RIS. As the two eddy

148   features moved away from the RIS into the Ross Sea interior, they became more clearly

149   evident in ocean color imagery as local minima in Chl-a (Fig. 3b).

150

151   2.2 High-resolution survey of the RIS eddies

152   Voyage NBP-1201of RVIB *Nathaniel B. Palmer* took place from December 24, 2011

153   to Feb 5, 2012. A multi-scale survey of the Ross Sea was carried out, and herein we focus

154   on a subset of the observations collected in the vicinity of the RIS. High-resolution

155   cross-sections of Eddies 1 and 2 were obtained with the Video Plankton Recorder (VPR;

156   Davis et al., 1992), providing conductivity, temperature and depth (CTD) observations,

157   along with fluorescence measurements and plankton imagery. Underway Acoustic

158   Doppler Current Profiler (ADCP) current velocity observations were collected along the

159   ship track with an RD Instruments NB150. Temperature, salinity, and fluorescence

160   profiles were obtained with a SeaBird Electronics 911 CTD and standard Rosette system.

161   A VPR survey of Eddies 1 and 2 was conducted on January 26 (magenta line, Fig. 3).

162   The ship track started from the west and cut through Eddy 1. It then passed across the

163   frontal area between the two eddies, penetrated into the interior of Eddy 2, and

164   subsequently turned southeastward. Along-track ADCP data suggests that both eddies are

165   anticyclonic (counterclockwise rotation), although the eastern flank of Eddy 2 was not

166   surveyed and thus the closed circulation of that feature cannot be validated. Also note that

167   the eddies were moving fast enough that we do not expect exact matchup of the *in situ*

168   observations with the satellite image due to differences in timing- e.g., the northward

169   swirl on the eastern flank of Eddy 1 observed with the shipboard ADCP is outside the

170   eddy core depicted in the satellite data. The VPR data revealed that the cores of both

171   eddies contained low-salinity lenses extending from the surface to 80-120 m (Fig. 4b).

172   The surface layer temperature was 0.6 ºC lower than outside of the eddies (Fig 4a). The

173   mixed layers within the eddies were deeper than outside, where the surface layer of

174   relatively warm and salty water was only about 45 m deep (Fig. 4a, b). The cold and fresh

175   lenses in the eddy interiors contained higher fluorescence than ambient waters sampled

176   west of Eddy 1 (Fig. 4c), consistent with high abundance of *P. antarctica* colonies

177   identified in the VPR imagery (Smith et al., submitted). Highest fluorescence along the

178   ship track occurred at the frontal boundary on the western flank of Eddy 2 (where the

179   flow is southward as suggested by along-track ADCP, Fig. 3), although the mechanism

180   responsible for that submesoscale enhancement of fluorescence remains unknown.

181   It is interesting to note that the lenses of high fluorescence revealed by the VPR data

182   (Fig. 4c, d) were manifested as local minima in Chl-a in the satellite imagery (Fig. 3).

183   Caution needs to be taken in comparing *in situ* fluorescence and satellite data for several

184   reasons. First, the algorithm for retrieving MODIS Chl-a is based on water leaving

185   irradiance (Clark, 1997), and the Chl-a concentration reflects a weighted average over the

186   upper 1-2 optical depths. Second, remotely sensed Chl-a can also be contaminated by

187   other dissolved and particulate materials (Carder et al., 2004). Third, *in situ* fluorescence

188   can be reduced by the 'quenching effect' (e.g., Falkowski et al., 1995) when

189   photosynthetic reaction centers are saturated with ambient light, such as typically occurs

190   in the upper euphotic zone when daylight is abundant, which was always the case during

191   the cruise season.

192   Despite these caveats, it is still of interest to make direct comparisons between the

193   VPR observations of fluorescence and the satellite retrievals of Chl-a. In order to

194   compare the VPR observations with satellite data, one needs to take into account the

195   vertical extent over which the satellite observations pertain. The optical depth can be

196   estimated based on an inverse relationship with the attenuation coefficient of downward

197　irradiance (K_d) for blue light (http://oceancolor.gsfc.nasa.gov/cms/atbd/kd_490). Based

198　on satellite data from January 2012, K_d was within the range of 0.2-0.4 m^{-1} near the RIS

199　edge (not shown), indicating an optical depth of ~5 m. Comparison of the VPR

200　fluorescence averaged over upper two optical depths (10 m) and the satellite-based Chl-a

201　concentration extracted along the VPR transect reveals similarity between two variables

202　(Fig. 4d). Both VPR fluorescence and MODIS Chl-a were highest near the frontal region

203　between the two eddies. Clearly, the satellite observations do not reflect the deeper

204　structure of the fluorescence distribution (Fig. 4c) which results in local maxima of

205　depth-integrated fluorescence located at the center of Eddy 1 and at the frontal boundary

206　in between the two eddies (Fig. 4d).

207
208　2.3 CTD transects

209　　　　On January 25-26, 2012, two CTD transects were conducted: one along the edge

210　(within several kilometers) of the RIS, and one normal to it (Fig. 3). In general, waters

211　along the RIS tended to be colder and fresher than those to the north (Fig. 5). However,

212　there was considerable variability in properties along the ice shelf. At station 62, there

213　was a cold and fresh layer extending to nearly 150m, with patchy fluorescence

214　throughout that interval. This vertical structure is reminiscent of that observed in the

215　interiors of Eddies 1 and 2, with very similar temperature and salinity characteristics.

216

217　**3. Model configuration**

218　　　　The Regional Ocean Modeling System (ROMS, Haidvogel et al., 2008; Shchepetkin

219　and McWilliams, 2005) is used in this study. ROMS is a free-surface, hydrostatic,

220　primitive-equation model that employs split-explicit separation of fast barotropic and

221　slow baroclinic modes and vertically stretched terrain-following coordinates. An ice shelf

222　module is coupled with the ocean model (Dinniman et al., 2011; Stern et al., 2013). The

223　*K*-profile parameterization (KPP) turbulence closure scheme (Large et al., 1994) is

224　applied to compute both momentum and tracer vertical mixing. The KPP scheme is

225   modified according to Dinniman et al. (2003), which prevents the mixed layer from

226   unrealistic shallowing during stratified conditions. Sensitivity tests show that altering

227   values for horizontal diffusivity within reasonable ranges have limited impact on the

228   major conclusions herein (Appendix A). Quadratic drag is used to compute the frictional

229   force on water in contact with the bottom and the ice shelf. The model also includes

230   mechanical and thermodynamic interactions between the floating ice shelf and water

231   cavity underneath (Holland and Jenkins, 1999; Dinniman et al., 2011; Stern et al., 2013).

232   A brief description on the parameterization of the ice shelf basal melting is provided in

233   Appendix B. Interested readers are referred to Dinniman et al. (2011) for additional

234   details of the model.

235

236   3.1 Model grid and ice shelf

237   Our idealized 2-D and 3-D models of the RIS utilize the same cross-shelf geometry,

238   configured to mimic the average bottom elevation and ice shelf draft in Bedmap2

239   (Fretwell et al., 2013) data for the area of interest (Fig. 6). This configuration is similar to

240   that used in another idealized modeling study (Gwyther et al., 2015). It reflects a

241   representative average of the many years the data that were collected to form Bedmap2,

242   rather than the specific details of the geometry present in January 2012 when the eddies

243   of interest were observed. Both our 2D and 3D models have 100 vertical layers, and

244   horizontal grid resolution of 500 m in the along-ice shelf and cross- ice shelf direction

245   (referred to as the X- and Y-directions, respectively). The horizontal resolution is

246   approximately one order of magnitude smaller than the first baroclinic Rossby radius of

247   deformation, thus making it suitable for simulating eddy processes at an ice shelf front

248   (Årthun et al., 2013). The bottom is flat with a depth of 600 m. The model domains span

249   500 km in the cross- ice shelf direction in order to minimize impacts of the open offshore

250   boundary on the processes of interest near the ice shelf. The 3-D model domain spans 100

251   km in the along- ice shelf direction. See Appendix B for additional information pertaining

10

252   to accuracy of the pressure gradient calculation in this particular geometry.

253

254   3.2 Initial and boundary conditions

255   Both initial and boundary conditions (Fig.6) are spatially uniform based on the

256   vertical temperature and salinity profiles from CTD station 58, the most offshore station

257   for the RIS CTD survey (Fig. 5). This site was chosen to reflect ambient conditions,

258   outside of the immediate influence of the ice shelf. Initial velocities and sea level

259   elevations are set to zero. The selection of the initial condition is *ad hoc*, as the

260   hydrographic conditions near the edge of the ice shelf were not sampled extensively.

261   Some of the uncertainties associated with the initial condition are assessed in section 6.

262   A closed wall is imposed on the southern boundaries of the model domains. In the

263   north, open boundary conditions are applied to tracers following the method of

264   Marchesiello et al. (2001), with the external values provided by CTD station data. At the

265   open northern boundary of both models, a 20-point sponge layer provides enhanced

266   viscosity and diffusivity to suppress numerical noise generated by wave reflection. The

267   2-D model actually includes six grid points in the along- ice shelf direction, but periodic

268   boundary conditions yield a solution that is effectively 2-D. Periodic boundaries are also

269   used in the 3-D model, but its 100 km extent in the along- ice shelf direction allows

270   energetic mesoscale flows to develop. No tidal forcing is included in the model.

271

272   3.3 Surface forcing

273   Wind forcing is from the Antarctic meteorological station VITO on the Ross Ice Shelf

274   (Fig. 1). The three hourly wind speed from VITO is converted to wind stress based on the

275   formulation of Large and Pond (1981), and the wind forcing is assumed to be spatially

276   uniform over the entire model domain. We compared the VITO record (Fig. 7) with

277   shipboard wind measurements during the time period when the RIS area was being

278   sampled (January 23-26). Both sources indicated southerly flow during that period,

279   although the winds measured at sea were at times up to 50% stronger (not shown). This

280   comparison confirms the VITO winds are appropriate forcing for the model simulations;

281   the impact of the apparent increase in winds over the ocean is addressed in sensitivity

282   experiments described in Section 5. There is no surface flux of fresh water. A constant

283   surface net heat flux of 35 W m^{-2} into the ocean is specified, which is the mean value for

284   the month of January from the 3-D model simulations of the Ross Sea described in

285   Dinniman et al. (2011). As we are simulating summer ice-free conditions, the sea ice

286   module available in ROMS is turned off.

287

288   3.4 Ross Ice Shelf edge roughness in the 3-D model

289   To implement realistic roughness in the edge of the RIS, we first digitized the edge

290   from the Bedmap2 ice thickness (http://nora.nerc.ac.uk/501469/). Second, those

291   roughness elements were projected onto the straight ice shelf edge in our idealized

292   geometry. The characteristic ice shelf edge roughness length scales of 5-20 km (Fig. 8c-f)

293   are well resolved by the 1 km resolution Bedmap2 database. These roughness scales are not

294   inconsistent with those present in the MODIS imagery (Figs. 2 and 3). This suggests that

295   roughness derived from Bedmap2 is suitably realistic, despite being derived from a

296   longer-term average rather than an instantaneous snapshot.

297

298   **4. Numerical simulation of RIS eddies**

299   Both satellite imagery and the *in situ* VPR observations documented the presence of

300   the cold and fresh eddies near the RIS edge. It is therefore of interest to explore the

301   generation mechanisms responsible for their formation. To do this, we design three

302   experiments evaluating the relative importance of three factors: ice shelf roughness, basal

303   melting, and surface wind stress (Table 1). Except where otherwise noted, the 3-D

304   simulations are run for 25 days.

305   The baseline case includes a straight ice shelf, wind forcing, and basal melting (run

306   SIS+WIND+BM). Our basal melt rate for the ice shelf front (between 6-16 km of the ice

307   shelf edge) in the model is 1.0 ± 0.4 m yr^{-1}, similar to the estimate by Arzeno et al. (2014)

308   using mooring observations (1.2 ± 0.5 m yr^{-1}). The estimated basal melt rate between 1-5

309   km of the ice shelf edge from our model is 3.2 ± 0.9 m yr^{-1}, and is comparable to the estimate

310   of Horgan et al. (2011) for that region based on satellite altimetry ($\sim2.1\pm0.9$ m yr^{-1}).

311   A cold and fresh boundary layer forms at the edge of the ice shelf due to basal

312   melting, generating a baroclinic jet (Fig. 8 a, b), a feature similar to that described by

313   Niebauer (1982) for a marginal sea ice edge. This is also consistent with a westward

314   coastal jet found near the RIS front (Jacobs et al., 1970; Keys et al., 1990). Variations in

315   surface velocity in the interior of the model domain away from the baroclinic jet at the

316   edge of the ice shelf are driven by wind forcing. In this experiment, we see no evidence

317   for generation of the types of mesoscale structures we observed (Figs. 2 and 3), even

318   when the model was run out for an additional 60 days (not shown).

319   When the straight ice shelf is replaced with an irregular one (run IIS+WIND+BM),

320   mesoscale instabilities develop in the boundary current, shedding cold and fresh eddies

321   into the interior (Fig. 8 c, d). The eddies are larger than the spatial scale of ice shelf

322   irregularities, and therefore the eddy structure is not expected to be set by the ice shelf

323   roughness. Indeed, we expect the eddy scale to be related to the Rossby radius of

324   deformation. We performed a sensitivity experiment in which the amplitude of the

325   roughness perturbations was reduced to 1/8 of the realistic case, and found similar sized

326   eddies were created on the same time scales (not shown). This suggests that our results are

327   not particularly sensitive to the details of the specified roughness.

328   To quantify the importance of wind forcing, the experiment was repeated with wind

329   forcing turned off (run IIS+BM). Instability in the boundary current persists (Fig. 8 e, f),

330   generating cold and fresh eddies similar those present in run IIS+WIND+BM (Fig. 8 c, d).

331   Thus wind forcing is not necessary for eddy formation, although it does make the

332   resulting eddies more energetic (Cf. Figs. 8c, d and 8e, f), with a domain-wide eddy

333   kinetic energy 60% larger than the no-wind case at model day 25. Additional experiments

334   were conducted to determine the degree to which the results were sensitive to the phasing

335   of the wind fluctuations. This was accomplished by starting the simulations at different

336   times during the wind record. Although the detailed evolution of the eddy field differed as

337   a result of these variations in forcing, the qualitative behavior was unchanged.

338   We note that temperatures in these simulations are higher than observed (Cf. Figs. 3,

339   8). The model is initialized with temperature and salinity profiles observed during the

340   field survey (January 25), and we apply a constant surface heat flux (35 W m^{-2})

341   throughout the simulations. It is therefore not surprising that the simulated temperature is

342   higher than observed. Our idealized simulations are aimed at understanding eddy

343   formation mechanisms, rather than hindcasting the specifics of the observed conditions.

344   Pawlak and McCready (2002) conducted laboratory experiments to study the

345   instabilities associated with oscillatory flow. Their results showed that oscillatory flow

346   along an irregular coastline can change streamlines and vorticity, thus providing a

347   mechanism for transferring anomalies from the boundary to the interior of the flow. The

348   instability and eddies are further found to be linked to the along-shore flow length scale

349   and roughness length scale, a finding consistent with numerical simulations of Signell

350   and Geyer (1991). With a rougher ice edge with smaller length scale, a stronger

351   eddy-driven flow is present. In our case, a similar mechanism exists. The formation of

352   cold and fresh anomalies due to basal melting first generates an along-shelf flow. The

353   resulting baroclinic current is perturbed by irregular ice shelf edge, triggering instability

354   that forms eddies, which carry the cold and fresh anomalies offshore to the open ocean.

355   The inclusion of wind forcing, though, can modulate the instabilities through

356   wind-induced oscillations in cross- ice shelf flow, thus further changing the timing and

357   detailed structure of eddies. Chu (1987) studied the fast ice-ocean interaction, and found

358   that even without any prescribed external forcing, the most unstable vertical wave mode

359   can be excited by curvatures in the ice edge, which is also consistent with our conclusion

360   here.

361   To compare with the observed eddies that are separated from the ice shelf on January

362   25, we sample a cross-section of one of the eddies simulated in run IIS+WIND+BM (Fig.

363   8cd). It reveals a lens of cold and fresh water is present in the upper 35 m (Fig. 9).

364   Although the hydrographic structure of the simulated eddy is qualitatively similar to

365   observations, the thickness of the lens is much less than indicated by the VPR survey (Fig.

366   4). Mechanisms for thickening the lens of cold and fresh water are the subject of the next

367   section.

368

369   **5. 2-D model simulations**

370   We showed that the cold eddy formation is facilitated by ice shelf roughness and

371   basal melting. Since the thick lenses are observed both within the mesoscale RIS eddies

372   as well as at the RIS edge where the eddies originate, it would therefore be of interest to

373   understand what controls the surface lens thickening at the edge of the ice shelf.

374   For this purpose, a series of 2-D model sensitivity experiments are carried out with

375   simulations running for 30 days (Table 2). In the first experiment (run WIND), the model

376   is forced by wind only. A strong downwelling-favorable wind event during January 22-28

377   (Fig. 7) forms a thick layer of relatively warm and fresh waters adjacent to the RIS,

378   composed of surface waters drawn in from offshore and downwelled at the ice edge (Fig.

379   10 a, f, k). Although the salinity of the downwelled fluid is low, it is not as low as

380   observed (Fig. 5), suggesting glacial melt is involved in freshening of the waters adjacent

381   to the RIS. In the second case (run BM), the wind forcing is turned off and basal melting

382   is turned on. Buoyant convection of meltwater from the underside of the ice shelf leads to

383   a cold and fresh layer adjacent to the RIS that depresses the pycnocline by a few tens of

384   meters (Fig. 10 b, g, l). Offshore of this boundary layer, strong stratification develops in

385   surface waters owing to the surface heat flux and lack of turbulent kinetic energy input

386   from the wind. In the third case (run WIND+BM), the combination of wind forcing and

387   basal melt creates a thick (~65 m) lens of cold and fresh water adjacent to the ice shelf

15

388   (Fig. 10 c, h, m). With wind forcing restored, stratification of the waters north of the ice

389   shelf is similar to that of the first experiment (Cf. Fig. 10 a, f, k and c, h, m).

390   Although run WIND+BM generates a layer of cold and fresh water reminiscent of

391   that observed near the ice shelf (Fig. 5), it is not as thick. Two more sensitivity

392   experiments are conducted to assess whether or not this discrepancy between the

393   simulated and observed distributions could be explained by differences in the forcing and

394   initial conditions. First, the wind stress was increased by 50% (run HWIND+BM, Fig. 10

395   d, i, n). This causes a modest deepening of the cold fresh layer, from ~65 m in run

396   WIND+BM to ~75 m in run HWIND+BM. Second, as the initial condition is rather *ad*

397   *hoc* due to limited observations available near ice shelf edge, the temperature, salinity,

398   and density fields in the initial condition were made constant below 50 m, with the

399   observed wind forcing applied (run WIND+BM+WS, Cf. Fig.10 e, j, o and c, h, m). This

400   reduction in the stratification allows the cold and fresh layer to deepen to 150 m (below

401   the vertical interval shown in Fig. 10). By reducing the buoyancy Richardson number, the

402   same input of turbulent kinetic energy can homogenize a thicker layer of the upper water

403   column (Abarbanel et al., 1984), thus providing more deepening of the mixed layer by

404   the same amount of surface stress (Trowbridge, 1992).

405

406   **6. Discussion**

407   The 3-D numerical experiments highlight the role of irregularities in the geometry

408   of the ice shelf edge in stimulating eddy formation. The propagation of these eddies away

409   from the RIS can facilitate the lateral transport of glacial meltwater and *P. antarctica*

410   blooms into the interior of the Ross Sea. Our results are consistent with the previous

411   findings by Chu (1987), which showed in a semi-analytical framework that unstable

412   wave modes can be excited by along-ice shelf curvatures. This mechanism of eddy

413   formation is also similar to that found in tidal regimes. Both numerical models (Signell

414   and Geyer, 1992) and laboratory observations (Pawlak and MacCready, 2002), illustrate

415   how irregularities in geometry such as ridges and/or headlands can facilitate flow

416   separation, causing vortices to be injected into the ocean interior. The origin of the cold

417   and fresh near-surface layer adjacent to the RIS can be attributed to basal melting, as

418   evidenced by comparison of the 2-D experiments with and without this effect. However,

419   the properties of this lens may be influenced by other processes not simulated by the

420   model. For example, formation of frazil ice can make the ice shelf water even more

421   buoyant (Jenkins and Bombosch, 1995; Smedsrud and Jenkins, 2004). Moreover, along-

422   ice shelf variability in the RIS plume may be driven by a host of factors, including spatial

423   variations in the cavity geometry, atmospheric forcing, and basal melting rate.

424   Downwelling-favorable winds were shown to be an important agent of thickening the

425   near-surface lens of cold and fresh water at the edge of the ice shelf. In order to ascertain

426   the degree to which such conditions may prevail at the RIS during summertime, we

427   compute the cumulative upwelling index for each January during the period 2010-2014.

428   First, the upwelling index (UI) is computed according to UI$=\frac{\tau_x}{\rho f}$ (i.e., the offshore

429   component of the Ekman transport) following the method of *Schwing et al.* (1996), where

430   τ_x is the alongshore component of wind stress calculated using the Large and Pond (1981)

431   scheme, and *f* is the local Coriolis parameter. Positive (negative) UI represents upwelling

432   (downwelling) favorable wind conditions. The cumulative UI (CUI) is then computed by

433   integrating the resulting UI over time (i.e., $CUI=\int UI\,dt$) between January 1 and January

434   31 of each year. The slope of CUI is particularly informative, in that the most

435   downwelling-favorable wind conditions are represented by the steepest descending trend

436   shown in CUI. In contrast, a rising trend in CUI indicates that upwelling-favorable wind

437   (negative UI) becomes more dominant.

438   All Januaries in the time period examined exhibited downwelling-favorable wind

439   conditions (Fig. 11). However, there is significant interannual variability—and our

440   observations were collected during a time period when the downwelling-favorable aspect

441   of the wind was relatively modest. We therefore conclude that wind-forced thickening of

442   the cold and fresh layer may be a frequent occurrence in this regime. However, other

443   mechanisms such as variations in the basal melting rate could be as important or perhaps

444   even more so.

445

446   **7. Summary and Conclusions**

447   *In situ* observations along with numerical model simulations were used to investigate

448   the dynamics of cold and fresh eddies near the edge of the Ross Ice Shelf that contained

449   high phytoplankton biomass, dominated by *P. antarctica*.

450   Idealized 3-D model simulations were able to generate eddies near the RIS with

451   properties similar to those observed. Sensitivity experiments showed that basal melting

452   can produce a cold and fresh plume adjacent to the RIS, which accelerates a baroclinic

453   current. In the presence of irregularities in the edge of the ice shelf, that current becomes

454   unstable and sheds eddies with the cold and fresh water mass properties of the plume.

455   The plume is consistent with previous findings of Niebauer (1983), and the eddy

456   formation mechanism is similar to results from previous numerical simulations (Chu et

457   al., 1987; Signell and Geyer, 1992) and laboratory experiments (Pawlak and McCready,

458   2002). However, in our simulations the cold and fresh lenses were quantitatively

459   shallower than observed by VPR (35 m vs. 80 m). Idealized 2-D model simulations were

460   then used to investigate the processes that can deepen the cold and fresh surface layer

461   adjacent to the RIS. Wind-induced downwelling can deepen the layer, and the magnitude

462   of this effect depends on the strength of the wind and the underlying

463   stratification—neither of which are particularly well constrained by available data.

464   Sensitivity experiments using the 2-D model document that plausible perturbations to the

465   wind stress and stratification can result in formation of a cold and fresh layer with a

466   vertical extent similar to that observed near the edge of the RIS and in the RIS eddies. A

467   follow-up 3-D simulation with reduced stratification produces thicker lenses within the

468   simulated eddies (not shown). However, we note that the observations document

469   substantial along- ice shelf variability in the density structure. Thus, the thickness of the

470   cold and fresh layer entrained into RIS eddies will vary depending on ambient conditions

471   present at the time of eddy formation. Although our idealized 3-D simulations did not

472   produce eddies with lenses as thick as those observed, we expect that a model with more

473   realistic along- ice shelf variability in water masses, subsurface ice shelf-roughness,

474   stratification, and surface forcing (wind and heat flux) would do just that. Lateral fluxes

475   associated with these eddies may be important in transporting physical, chemical and

476   biological properties from the RIS into the interior Ross Sea.

477

References

Abarbanel, H. D., Holm, D. D., Marsden, J. E., and Ratiu, T., 1984. Richardson number criterion for the nonlinear stability of three-dimensional stratified flow. Phys. Rev. Lett., 52, 2352.

Arrigo, K. R., Worthen, D., Schnell, A., and Lizotte, M. P., 1998, Primary production in Southern Ocean waters. J. Geophys. Res., 103, 15587-15600.

Arrigo, K.R., Worthen, D.L. and Robinson, D.H., 2003. A coupled ocean‑ecosystem

508   model of the Ross Sea: 2. Iron regulation of phytoplankton taxonomic variability and
509   primary production. J. Geophys. Res. Oceans, 108(C7).
510 Arrigo, K. R., van Dijken, G. L., and Strong, A. L. 2015, Environmental controls of
511   marine productivity hot spots around Antarctica. J. Geophys. Res. Oceans,
512   10.1002/2015JC010888.
513 Årthun, M., Holland, P. R., Nicholls, K. W., & Feltham, D. L., 2013. Eddy-Driven
514   Exchange between the Open Ocean and a Sub–Ice Shelf Cavity. J. Phys. Oceanogr.,
515   43-11, 2372-2387.
516 Arzeno, I. B., R.C. Beardsley, R. Limeburner, B. Owens, L. Padman, S. R. Springer, C. L.
517   Stewart, and M. JM., Williams, 2014. Ocean variability contributing to basal melt
518   rate near the ice front of Ross Ice Shelf, Antarctica. J. Geophys. Res. Oceans, 119, 7:
519   4214-4233.
520 Carder, K. L., Chen, F. R., Cannizzaro, J. P., Campbell, J. W., and Mitchell, B. G., 2004,
521   Performance of the MODIS semi-analytical ocean color algorithm for chlorophyll-a.
522   Adv. Space Res., 33, 1152-1159.
523 Clark, D. K., 1997. Algorithm theoretical basis document–Bio-optical algorithms, Case I
524   waters, MODIS algorithm theoretical basis document 18, Version 1.2, available from:
525   http.modis.gsfc.nasa.gov/data/atbd/atbd mod18.
526 Clarke, A. J., 1978. On wind-driven quasi-geostrophic water movements near fast-ice
527   edges. Deep-Sea Res., 25, 41-51.
528 Chu, P., 1987. An air-sea feedback mechanism for quasi-geostrophic water movement
529   near a fast shelf-ice edge with a small curvature, Chinese J. Atmos. Sci. 11, 31-42.
530 Comiso, J.C., McClain, C.R., Sullivan, C.W., Ryan, J.P., Leonard, C.L., 1993. Coastal
531   Zone Color Scanner pigment concentrations in the Southern Ocean and relationships
532   to geophysical surface features. J. Geophys. Res., 98, 2419-2451.
533 Cushman-Roisin, B., Tang, B., & Chassignet, E. P., 1990. Westward motion of mesoscale
534   eddies. J. Phys. Oceanogr., 20, 758-768.
535 Davis, C. S., Gallager, S. M., Berman, M. S., Haury, L. R., and Strickler, J. R. ,1992. The
536   video plankton recorder (VPR): design and initial results. Arch. Hydrobiol. Beih, 36,
537   67-81.
538 Depoorter, M. A., Bamber, J. L., Griggs, J. A., Lenaerts, J. T. M., Ligtenberg, S. R. M.,
539   van den Broeke, M. R., and Moholdt, G. ,2013. Calving fluxes and basal melt rates
540   of Antarctic ice shelves. Nature, 502, 89-92.
541 Dinniman, M.S., J.M. Klinck and W.O. Smith, Jr., 2003. Cross-shelf exchange in a model
542   of the Ross Sea circulation and biogeochemistry, Deep-Sea Res. II, 50, 3103-3120.
543 Dinniman, M.S. and J.M. Klinck, 2004. A model study of circulation and cross-shelf
544   exchange on the west Antarctic Peninsula continental shelf, Deep-Sea Res. II, 51,
545   2003-2022.
546 Dinniman, M. S., J. M. Klinck, and W. O. Smith Jr., 2007. The influence of sea ice cover
547   and icebergs on circulation and water mass formation in a numerical circulation
548   model of the Ross Sea, Antarctica. J. Geophys. Res., 112, C11013,

549   doi:10.1029/2006JC004036.

550 Dinniman, M.S., J.M. Klinck and W.O. Smith, Jr, 2011. A model study of Circumpolar
551   Deep Water on the West Antarctic Peninsula and Ross Sea continental shelves.
552   Deep-Sea Res. II, 58, 1508-1523, doi: 10.1016/j.dsr2.2010.11.013

553 Dinniman, M.S., J.M. Klinck and E.E. Hofmann, 2012. Sensitivity of Circumpolar Deep
554   Water transport and ice shelf basal melt along the west Antarctic Peninsula to
555   changes in the winds. J. Clim., 25, 4799-4816.

556 Dumont, D., Gratton, and T. Arbetter, 2010. Modeling Wind-Driven Circulation and
557   Landfast Ice-Edge Processes during Polynya Events in Northern Baffin Bay. J. Phys.
558   Oceanogr., 40, 1356–1372. doi:10.1175/2010JPO4292.1

559 Erofeeva, S. Y., Padman, L., & Egbert, G. (2005). Assimilation of ship-mounted ADCP
560   data for barotropic tides: Application to the Ross Sea. Journal of Atmospheric and
561   Oceanic Technology, 22(6), 721-734.

562 Falkowski, P. G., and Kolber, Z. ,1995. Variations in chlorophyll fluorescence yields in
563   phytoplankton in the world oceans. Funct. Plant Biol., 22, 341-355.

564 Foldvik, A., & Kvinge, T. ,1974. Conditional instability of sea water at the freezing point.
565   Deep-Sea Res., 21, 3, 169-174.

566 Foster, T. D., 1983. The temperature and salinity fine structure of the ocean under the
567   Ross Ice Shelf. J. Geophys. Res., 88, 2556-2564.

568 Fretwell, P., et al. (2013). Bedmap2: improved ice bed, surface and thickness datasets for
569   Antarctica. The Cryosphere, 7.1.

570 Galton-Fenzi, B.K., 2009. Modelling Ice-Shelf/Ocean Interaction. Ph.D. thesis,
571   University of Tasmania, 151 pp.

572 Gerringa, L. J. et al., 2012. Iron from melting glaciers fuels the phytoplankton blooms in
573   Amundsen Sea (Southern Ocean): Iron biogeochemistry. Deep-Sea Res. II, 71,
574   16-31.

575 Gilmour, A. E., 1979. Ross ice shelf sea temperatures. Science, 203(4379), 438-439.

576 Gordon, A.L., A.H. Orsi, R. Muench, B.A. Huber, E. Zambianchi, and M. Visbeck, 2009.
577   Western Ross Sea continental slope gravity currents. Deep-Sea Res. II, 56, 796-817.

578 Goring, D.G., and Pyne, A., 2003. Observations of sea level variability in Ross Sea,
579   Antarctica. NZ J. Mar. Freshwater Res., 37: 241–249.

580 Gwyther, D. E., Galton-Fenzi, B. K., Dinniman, M. S., Roberts, J. L., & Hunter, J. R. ,
581   2015. The effect of basal friction on melting and freezing in ice shelf–ocean models.
582   Ocean Modell., 95, 38-52.

583 Haidvogel, D. B., Arango, H., Budgell, W. P., Cornuelle, B. D., Curchitser, E., Di
584   Lorenzo, E., ... and Wilkin, J. ,2008. Ocean forecasting in terrain-following
585   coordinates: Formulation and skill assessment of the Regional Ocean Modeling
586   System. J. Comput. Phys., 227, 3595-3624.

587 Häkkinen, S., 1986: Coupled ice-ocean dynamics in the marginal ice zones,
588   upwelling/downwelling and eddy generation. J. Geophysical Research, 91, 819–832.

589 Holland, D. M., and Jenkins, A., 1999. Modeling thermodynamic ice-ocean interactions

590   at the base of an ice shelf. J. Phys. Oceanogr., 29, 1787-1800.

591   Horgan, H.J., R.T. Walker, S. Anandakrishnan, and R.B. Alley, 2011. Surface elevation
592   changes at the front of the Ross Ice Shelf: Implications for basal melting. J. Geophys.
593   Res., 116, C02005.

594   Jacobs, S. S., Amos, A. F., & Bruchhausen, P. M., 1970. Ross Sea oceanography and
595   Antarctic bottom water formation. Deep-Sea Res., 17, 6, 935-962.

596   Jacobs, S. S., Gordon, A. L., and Ardai, J. L., 1979. Circulation and melting beneath the
597   Ross Ice Shelf, Science, 203, 439-443.

598   Jacobs, S.S., Fairbanks, R.G., and Horibe, Y., 1985. Origin and evolution of water masses
599   near the Antarctic continental margin: evidence from $H_2^{18}O/ H_2^{16}O$ ratios in seawater.
600   in: Oceanology of the Antarctic Continental Shelf (S. Jacobs, ed.), Antarct. Res, Ser.,
601   American Geophysical Union, Washington D.C., 43, 59-85.

602   Jacobs, S. S. (1992). Is the Antarctic ice sheet growing? Nature, 360, 29-33.

603   Jacobs, S. S., Hellmer, H. H., & Jenkins, A. ,1996. Antarctic ice sheet melting in the
604   Southeast Pacific. Geophys. Res. Lett., 23, 957-960.

605   Jacobs, S. S., Jenkins, A., Giulivi, C. F., and Dutrieux, P. ,2011. Stronger ocean
606   circulation and increased melting under Pine Island Glacier ice shelf. Nature Geosci.,
607   4, 519-523.

608   Jenkins, A., and Doake, C. S. M., 1991. Ice-ocean interaction on Ronne Ice Shelf,
609   Antarctica. J. Geophys. Res. Oceans, 96, 791-813.

610   Jenkins, A., and Bombosch, A., 1995. Modeling the effects of frazil ice crystals on the
611   dynamics and thermodynamics of ice shelf water plumes. J. Geophys. Res. Oceans,
612   100, 6967-6981.

613   Keys, H. J., Jacobs, S. S., and Barnett, D., 1990. The calving and drift of iceberg B-9 in
614   the Ross Sea, Antarctica. Antarctic Sci., 2, 243-257.

615   Klinck, J. M., Hofmann, E. E., Beardsley, R. C., Salihoglu, B., and Howard, S., 2004.
616   Water-mass properties and circulation on the west Antarctic Peninsula Continental
617   Shelf in austral fall and winter 2001. Deep-Sea Res. II, 51, 1925-1946.

618   Klinck, J. M., and M. S. Dinniman, 2010. Exchange across the shelf break at high
619   southern latitudes. Ocean Sci., 6, 513–524.

620   Krauss, E.B., Turner, J.S., 1967. A one-dimensional model of the seasonal thermocline.
621   Tellus 19, 98–105.

622   Large, W. G., and Pond, S., 1981. Open ocean momentum flux measurements in
623   moderate to strong winds. J. Phys. Oceanogr., 11, 324-336.

624   Large, W. G., McWilliams, J. C., and Doney, S. C., 1994. Oceanic vertical mixing: A
625   review and a model with a nonlocal boundary layer parameterization. Rev. Geophys.,
626   32, 363-404.

627   Losch. M., 2008. Modeling ice shelf cavities in a z coordinate ocean general circulation
628   model. J. Geophys. Res. Oceans, 113, C08043.

629   MacAyeal, D. R., 1984. Thermohaline circulation below the Ross Ice Shelf: A
630   consequence of tidally induced vertical mixing and basal melting. J. Geophys. Res.

Oceans, 89, 597-606.

MacAyeal, D. R., 1985. Tidal rectification below the Ross Ice Shelf, Antarctica. Antarct. Res. Ser., 43, 109-132.

Makinson, K., Schröder, M., & Østerhus, S., 2006. Effect of critical latitude and seasonal stratification on tidal current profiles along Ronne Ice Front, Antarctica. J. Geophys. Res., Oceans, 111, C03022.

Marchesiello, P., J.C. McWilliams, and A.F. Shchepetkin, 2001. Open boundary conditions for long-term integration of regional oceanic models. Ocean Modell., 3, 1-20.

Martin, J. H., 1990. Glacial‐interglacial CO2 change: The iron hypothesis. Paleoceanogr.y, 5(1), 1-13.

McGillicuddy, D.J., Sedwick, P.N., Dinniman, M.S., Arrigo, K.R., Bibby, T.S., Greenan, B.J.W., Hofmann, E.E., Klinck, J.M., Smith, W.O., Mack, S.L., Marsay, C.M., Sohst, B.M., and G.L. van Dijken ,2015. Iron supply and demand in an Antarctic shelf ecosystem, Geophys. Res. Lett., 42, 8088–8097.

Mellor, G. L., and Blumberg, A. F., 1985. Modeling vertical and horizontal diffusivities with the sigma coordinate system. Mon. Weather Rev., 113, 1379-1383.

Nicholls, K. W., Padman, L., Schröder, M., Woodgate, R. A., Jenkins, A., & Østerhus, S., 2003. Water mass modification over the continental shelf north of Ronne Ice Shelf, Antarctica. J. Geophys. Res. Oceans, 108, 3260.

Niiler, P.P., Kraus, E.B., 1977. One-dimensional models of the Upper Ocean. In: Krauss, E.B. (Ed.), Modeling and Prediction of the Upper Layers of the Ocean. Pergamon, New York, pp. 143–172.

Niebauer, H. J. ,1982. Wind and melt driven circulation in a marginal sea ice edge frontal system: a numerical model. Cont. Shelf Res., 1, 49-98.

Orsi, A.H., Smethie Jr., W.M., and Bullister, J.L., 2002. On the total input of Antarctic Waters to the Deep Ocean: a preliminary estimate from chlorofluorocarbon measurements. J. Geophys. Res. Oceans, 107, 3122.

Orsi, A.H. and Wiederwohl, C.L., 2009. A recount of Ross Sea waters. Deep Sea Research II, 56, 13-14, doi:10.1016/j.dsr2.2008.10.033.Pawlak, G., and MacCready, P., 2002. Oscillatory flow across an irregular boundary. J. Geophys. Res. Oceans, 107, 4-1.

Pawlak, G., & MacCready, P. 2002. Oscillatory flow across an irregular boundary. J. Geophys. Res. Oceans, 107(C5).

Pritchard, H. D., Ligtenberg, S. R. M., Fricker, H. A., Vaughan, D. G., Van den Broeke, M. R., and Padman, L. ,2012. Antarctic ice-sheet loss driven by basal melting of ice shelves. Nature, 484, 502-505.

Rignot, E., Jacobs, S., Mouginot, J., and Scheuchl, B., 2013. Ice-shelf melting around Antarct. Science, 341, 266-270.

Schwing, F. B., O'Farrell, M., Steger, J. M., and Baltz, K., 1996. Coastal Upwelling indices west coast of North America. NOAA Tech. Rep., NMFS SWFSC, 231, 144p.

672 Shchepetkin, A.F., McWilliams, J.C., 1998. Quasi-monotone advection schemes based on
673 explicit locally adaptive dissipation. Mon. Weather Rev., 126, 1541–1580.
674 Shchepetkin, A. F., & McWilliams, J. C., 2003. A method for computing horizontal
675 pressure-gradient force in an oceanic model with a nonaligned vertical coordinate. J.
676 Geophys. Res. Oceans, 108, 1-33.
677 Shchepetkin, A. F., and McWilliams, J. C., 2005. The regional oceanic modeling system
678 (ROMS): a split-explicit, free-surface, topography-following-coordinate oceanic
679 model. Ocean Modell. 9, 347-404.
680 Sedwick, P. N., G. R. DiTullio, and D. J. Mackey (2000), Iron and manganese in the Ross
681 Sea, Antarctica: Seasonal iron limitation in Antarctic Shelf Waters, J. Geophys. Res.
682 Oceans, 105(C5), 11321-11336.
683 Signell, R., P., and W. R., Geyer, 1991. Transient eddy formation around headlands. J.
684 Geophys. Res. Oceans, 96: 2561-2575.
685 Smedsrud, L. H., and Jenkins, A., 2004. Frazil ice formation in an ice shelf water plume.
686 J. Geophys. Res. Oceans, 109, C03025.
687 Smethie Jr., W.M. and Jacobs, S.S., 2005. Circulation and melting under the Ross Ice
688 Shelf: estimates form evolving CFC, salinity and temperature fields in the Ross Sea.
689 Deep-Sea Res. I, 52, 959-978.
690 Smith Jr, W. O., and D. J. McGillicuddy et al., Ghost colonies of *Phaeocystis*: distribution
691 and abundance in the Ross Sea, submitted, this issue.
692 Smith Jr, W. O., Ainley, D. G., Arrigo, K. R., & Dinniman, M. S. ,2014. The
693 oceanography and ecology of the Ross Sea. Ann. Rev. of Mar. Sci., 6, 469-487.
694 Stern, A. A., Dinniman, M. S., Zagorodnov, V., Tyler, S. W., and Holland, D. M. 2013.
695 Intrusion of warm surface water beneath the McMurdo Ice Shelf, Antarctica. J.
696 Geophys. Res. Oceans, 118, 7036-7048.
697 Trowbridge, J. H. ,1992. A simple description of the deepening and structure of a stably
698 stratified flow driven by a surface stress. J. Geophys. Res. Oceans, 97, 15529-15543.
699 Whitworth, T., and Orsi, A. H., 2006. Antarctic Bottom Water production and export by
700 tides in the Ross Sea. Geophys. Res. Lett., 33, L12609.

701

Appendix A. Model sensitivity to horizontal diffusivity

703 In numerical models, the background mixing coefficients are chosen based on grid

704 length scale and a time scale for energy dissipation. These parameters should be chosen

705 to preserve the dynamics of interest (Mellor and Blumberg, 1985), damping out

706 fluctuations that are not resolved by the grid (e.g. 2 Δx waves). In the harmonic case, the

707 background horizontal diffusivity is defined as $(\Delta x/\pi)^2/\Delta t$, where Δt is damping time

708 scale. Our grid resolution is Δx=500 m, so a practical range for Δt is 3~12 hours,

709   therefore resulting in a horizontal diffusivity coefficient of roughly 0.5~2 m^2s^{-1}. We

710   performed a series of experiments to test the sensitivity of lens thickness near the ice

711   shelf edge to this parameter. Results show that by changing viscosity from 0.5 to 4 $m^2\,s^{-1}$,

712   the lens thickness is only shallowed by ~2-3 meters, which is an order of magnitude or

713   more less than the amplitude of the simulated signal. In the simulations presented herein,

714   the diffusion coefficient is 0.5 m^2s^{-1}, a value that is smaller than that usually used with the

715   naturally dissipative upstream advection scheme (Shchepetkin and McWilliams, 1998;

716   Dinniman et al., 2003).

717

718   **Appendix B. Details for the basal melting and mechanical forcing by the ice shelf**

719   **edge**

720   Here we briefly summarize the representation of the ice shelf in the model. The

721   ocean water underneath has interactions with the ice shelf through thermodynamics.

722   Under the ice shelf, the upper boundary for the surface model layer is not at sea level

723   because it conforms to the ice shelf base. The hydrostatic pressure gradient force

724   calculation thus accounts for the possibilities that the top layer of the ocean may have a

725   significant slope due to the ice shelf (Shchepetkin and McWilliams, 2003), assuming that

726   the ice is in isostatic equilibrium. While there are concerns about pressure gradient (PG)

727   errors at the ice shelf front in terrain following coordinate models (e.g. Losch, 2008), the

728   PG algorithm used in ROMS (Shchepetkin and McWilliams, 2003) has been explicitly

729   shown to limit these issues in the case of ice shelf fronts (Galton-Fenzi, 2009). A 2-D run

730   without surface forcing or basal melting shows that the PG errors cause only small

731   perturbations to the density field. After several hours of simulation, the solution stabilizes.

732   Changes to the initial density field (~10^{-4} kg m^3) and the associated velocities (~10^{-6} m s^{-1})

733   are essentially small. This suggests that the PG error is not a problem in our simulations.

734   Atmospheric forcing of waters underneath the ice shelf is set to zero, assuming that

735   fluid is isolated from the atmosphere. Friction between the ice shelf and the water is

736   computed as a quadratic stress with a coefficient of 3.0×10^{-3}.

737   At the water-ice shelf interface, a viscous sublayer model is used with three

738   equations representing the conservation of heat, the conservation of salt, and a linearized

739   version of the formula for the freezing point of sea water as a function of salinity and

740   pressure. Free variables in these equations are T_b, S_b, and $\frac{\partial h}{\partial t}$, which stand for

741   temperature, salinity at the ice shelf base, and melting rate, respectively. $\frac{\partial h}{\partial t}$ is <0 for

742   melting and >0 for freezing.

743   The conservation of heat across the ocean-ice shelf boundary is:

744
$$\rho_i(L - C_{pi}\Delta T)\frac{\partial h}{\partial t} = \rho C_{pw}\gamma_T(T_b - T_w) \tag{B.1}$$

745   where ρ_i is ice density (930 kg m^{-3}), L is the latent heat of fusion (3.34×10^5 J kg^{-1}), C_{pi} is

746   the heat capacity of ice (2000 J (kg °C)$^{-1}$), and ΔT is the temperature difference between

747   the ice shelf interior and the freezing temperature at the ice shelf base. However, in our

748   simulations we did not consider the impact of heat conduction through the ice shelf,

749   therefore ΔT=0 and the ice shelf is assumed to be perfectly insulating. ρ is the density of

750   water, C_{pw} is the heat capacity of sea water at 0 °C (4000 J (kg °C)$^{-1}$), γ_T is the turbulent

751   exchange coefficient for heat and is computed as a function of the friction velocity

752   (Holland and Jenkins, 1999), and T_w is the water temperature in the uppermost grid box.

753   The conservation of salt across the ocean-ice shelf boundary is written as:

754
$$\rho_i S_b \frac{\partial h}{\partial t} = \rho \gamma_s(S_b - S_w) \tag{B.2}$$

755   where γ_s is the turbulent exchange coefficient for salt, and is computed as a function of

756   the friction velocity (Holland and Jenkins, 1999), and S_w is the salinity in the uppermost

757   grid box. The linearized equation for the freezing point of sea water (Foldvik and Kvinge,

758   1974) defines T_b as

759
$$T_b = 0.0939 - 0.057S_b + 7.6410 \times 10^{-4}h \tag{B.3}$$

760   where h is the depth below the sea level.

761   For simplicity, the draft and extent of the ice shelf do not change over time in the

762 model, a reasonable approximation for simulations of this duration also made in previous

763 simulations (Dinniman et al., 2007; Stern et al., 2013).

764

765

766

767

768

3-D experiments	Ice shelf edge	Basal melting	Surface wind forcing
SIS+WIND+BM	Straight	ON	ON
IIS+WIND+BM	Irregular	ON	ON
IIS+BM	Irregular	ON	OFF

769

770 Table 1. List of 3-D experiments performed in this study. In the left column, SIS and IIS

771 stand for "straight ice shelf" and "irregular ice shelf" respectively; BM stands for basal

772 melting.

773

774

2-D experiments	Basal melting	Surface wind forcing	Initial condition
WIND	OFF	Observed	CTD 58
BM	ON	OFF	CTD 58
WIND+BM	ON	Observed	CTD 58
HWIND+BM	ON	Observed ×1.5	CTD 58
WIND+BM+WS	ON	Observed	CTD 58, constant density below 50m

775

776 Table 2. List of 2-D experiments performed in this study. In the left column, HWIND,

777 WS, and BM stand for "high wind stress", "weak stratification", and "basal melting",

778 respectively.

779

780
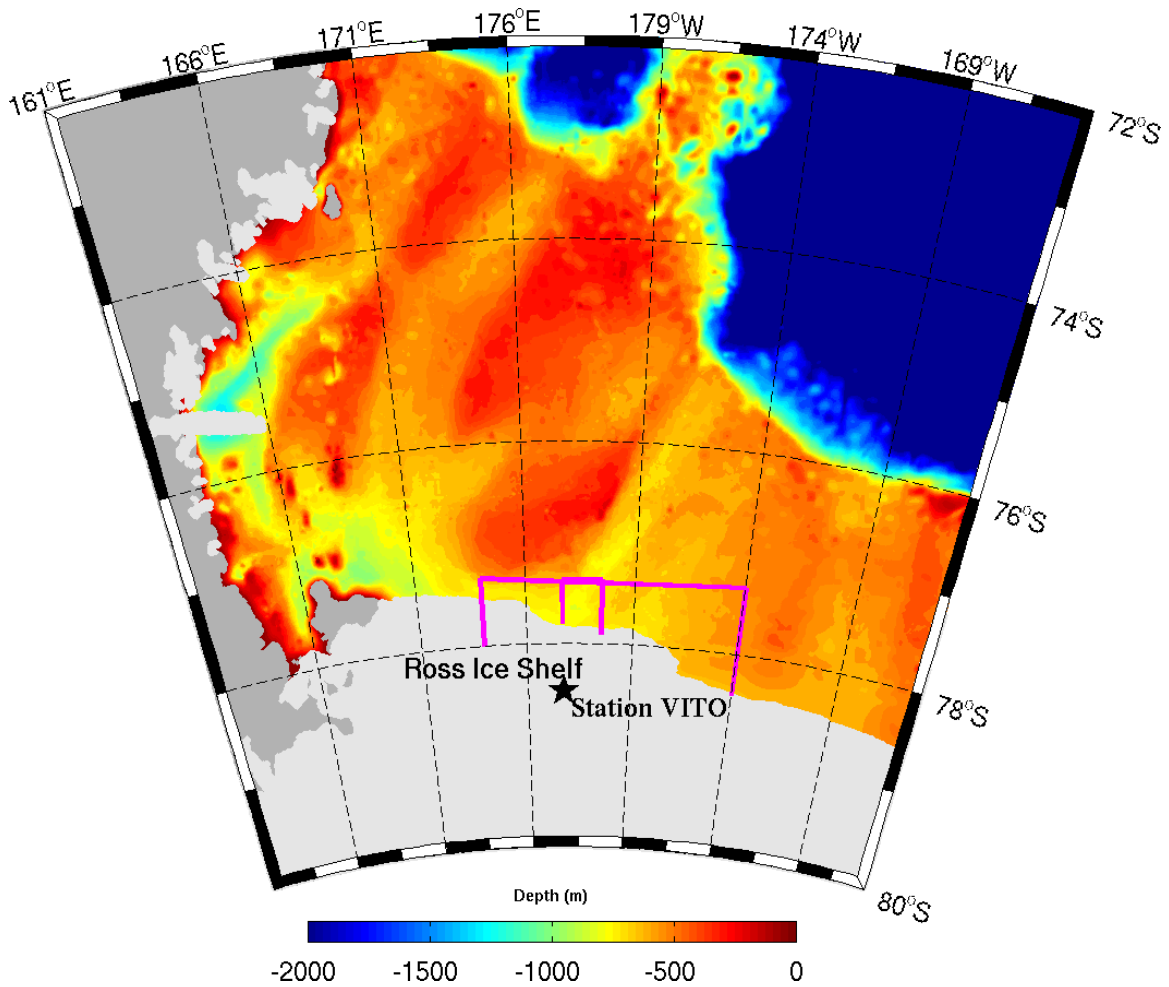
Fig. 1. Bathymetric map of the Ross Sea based on Bedmap2 bottom elevation data made available by the British Antarctic Survey (http://nora.nerc.ac.uk/501469/). White contours are the 400 m isobath. The Pentagram indicates the location for Antarctic meteorological station VITO. The permanent ice shelf is shown in light gray, and land in dark gray. Domains of the satellite images depicted in Figs. 2 and 3 are shown as solid magenta lines.

789
790
791

(a)
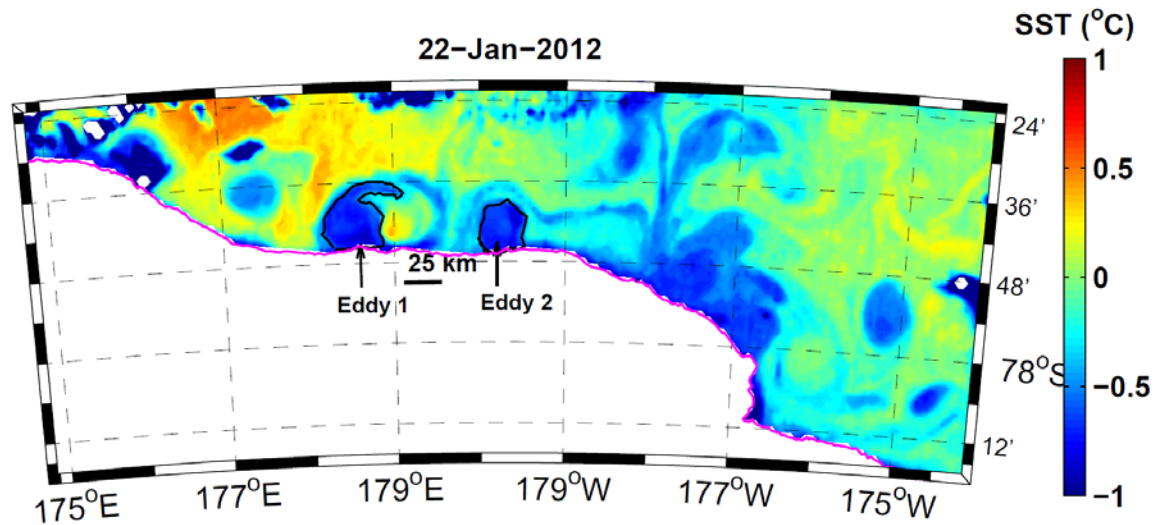
792
793

(b)
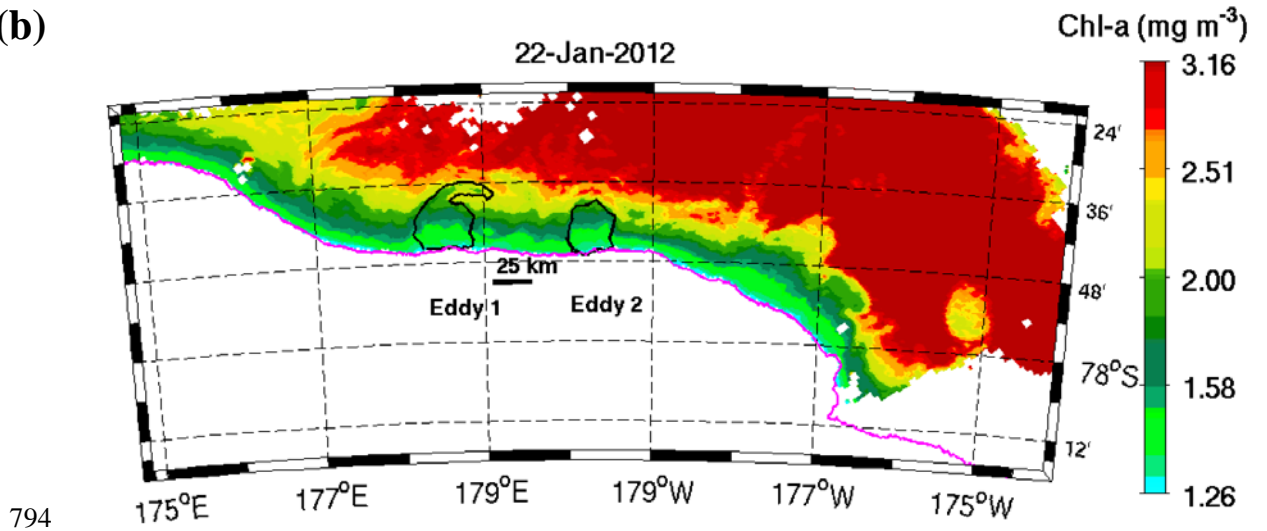
794

795
796 Fig. 2. Moderate Resolution Imaging Spectroradiometer (MODIS) level 2 (1 km
797 resolution) SST (panel a) and Chl-a (panel b) images for January 22, 2012. Black lines
798 outline the two ice shelf eddies, and magenta lines represent the ice shelf edge estimated
799 from MODIS true color image for January 2012. Satellite data provided by NASA's
800 Goddard Space Flight Center (http://modis.gsfc.nasa.gov/data/).
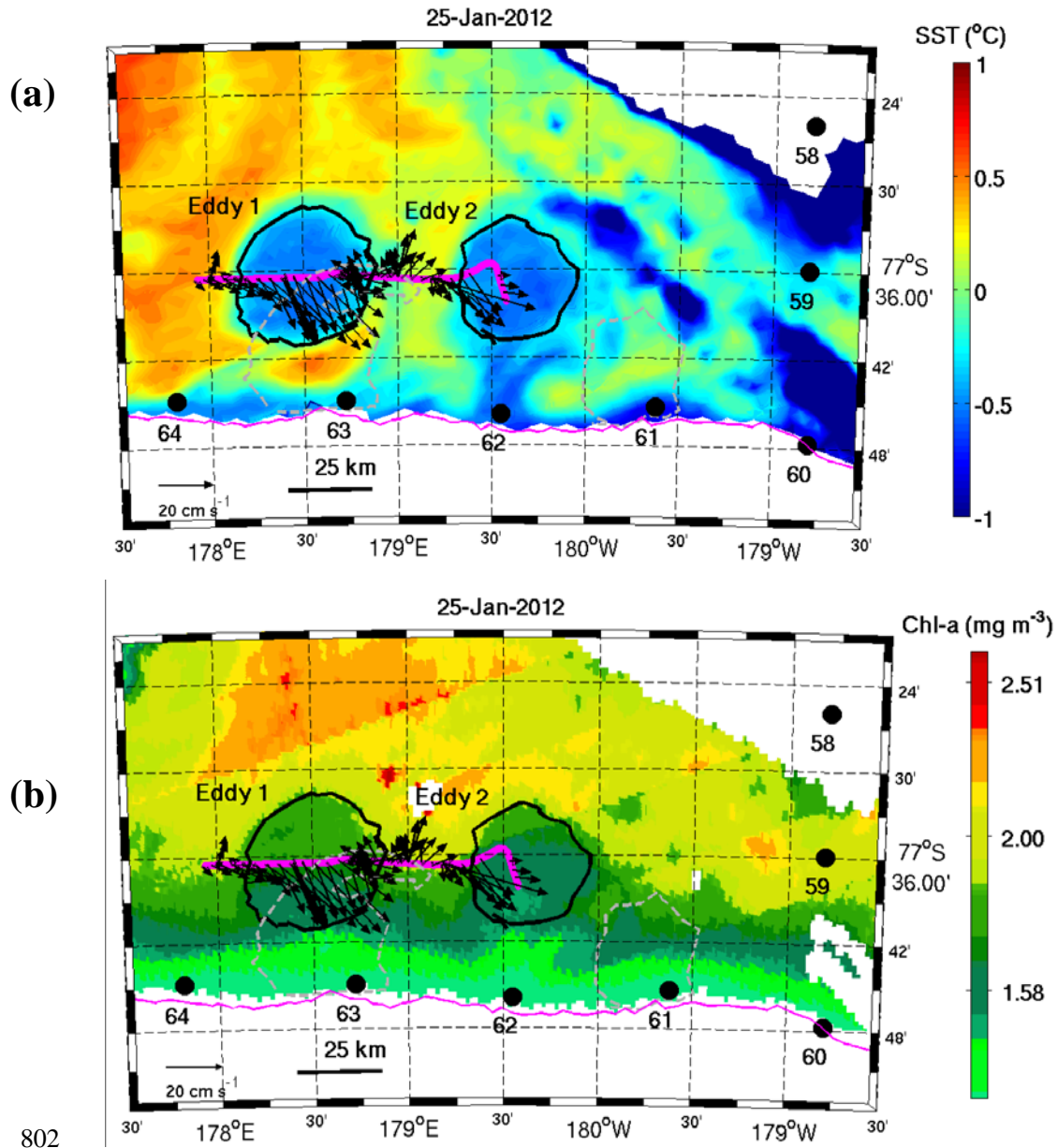
Fig. 3. Zoom in view of MODIS level 2 SST and Chl-a images for January 25, 2012.
Note that for visualization purposes, the Chl-a concentrations along swaths are projected
into a uniformly spaced longitude-latitude coordinate. The thick magenta lines indicate
the cross-eddy transect on January 26, 2012 depicted in Fig. 4, and thinner magenta lines
represent the ice shelf edge estimated from MODIS true color image for January 2012.
Black solid (gray dashed) lines outline the two ice shelf eddies on January 25 (22), and
black dots indicate CTD station locations (58-64) during the Ross Ice Shelf survey
January 25-26, 2012. Vectors stand for the depth-averaged current over top 150 m during
the survey. Tidal currents in this area are an order of magnitude smaller than the observed
current (Erofeeva et al., 2005) so the ADCP data have not been detided. Velocity scale
factor is shown at the lower left.

814

815
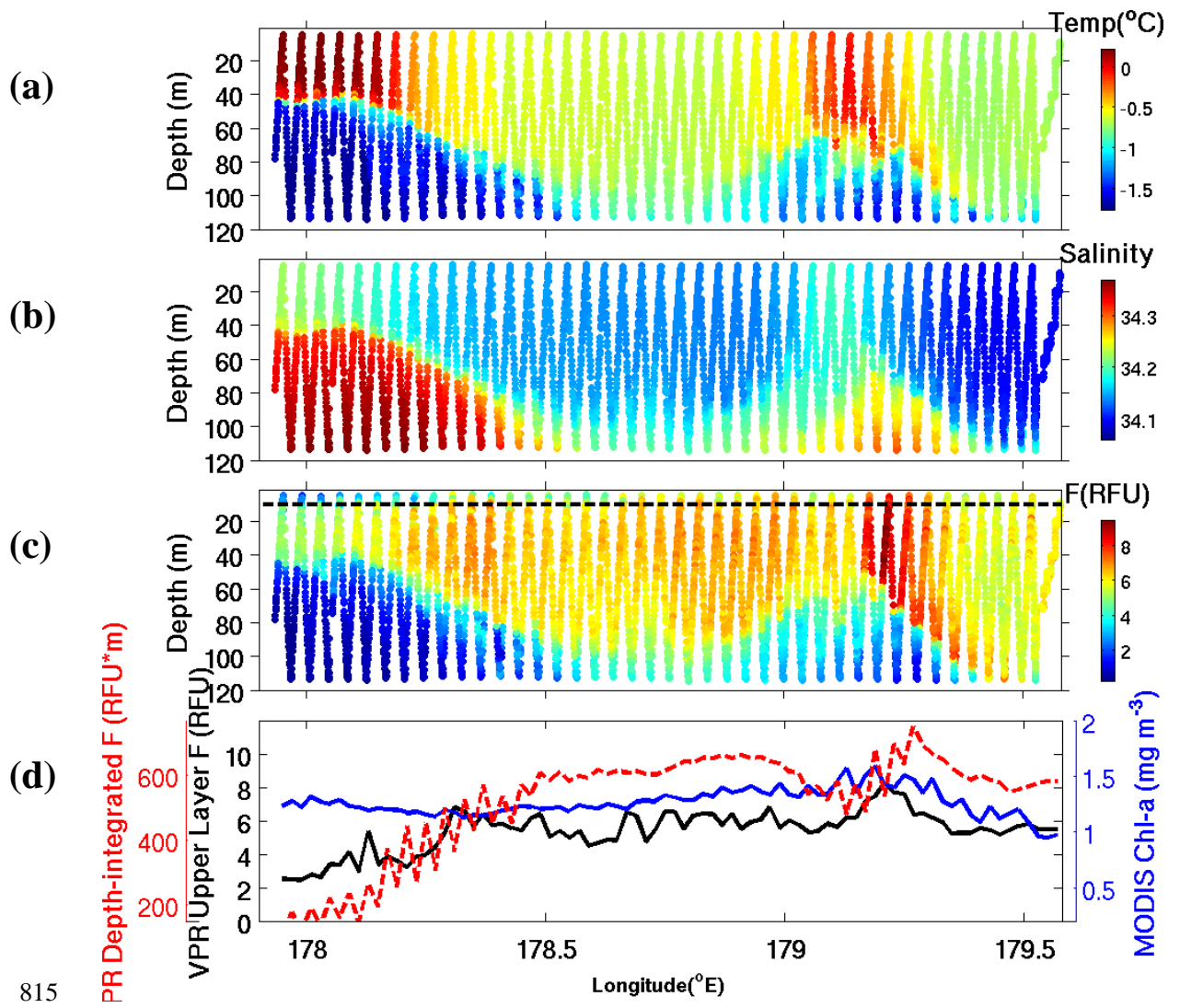
Fig. 4. Profiles of temperature, salinity and fluorescence (F). In panel (c), the depth of the second optical depth is plotted in black dashed line. F is in relative fluorescence units, or RFU. Note that this relative scale is not the same as that for the CTD observations presented in Fig. 5 from the VPR survey depicted by the magenta line in Fig. 3. Bottom panel shows the weighted VPR fluorescence within the top 10 m (black), MODIS surface Chl-a concentration extracted along the VPR track (blue), and depth-integrated VPR fluorescence (red) within the top 100m.

816
817
818
819
820
821
822
823
824
825
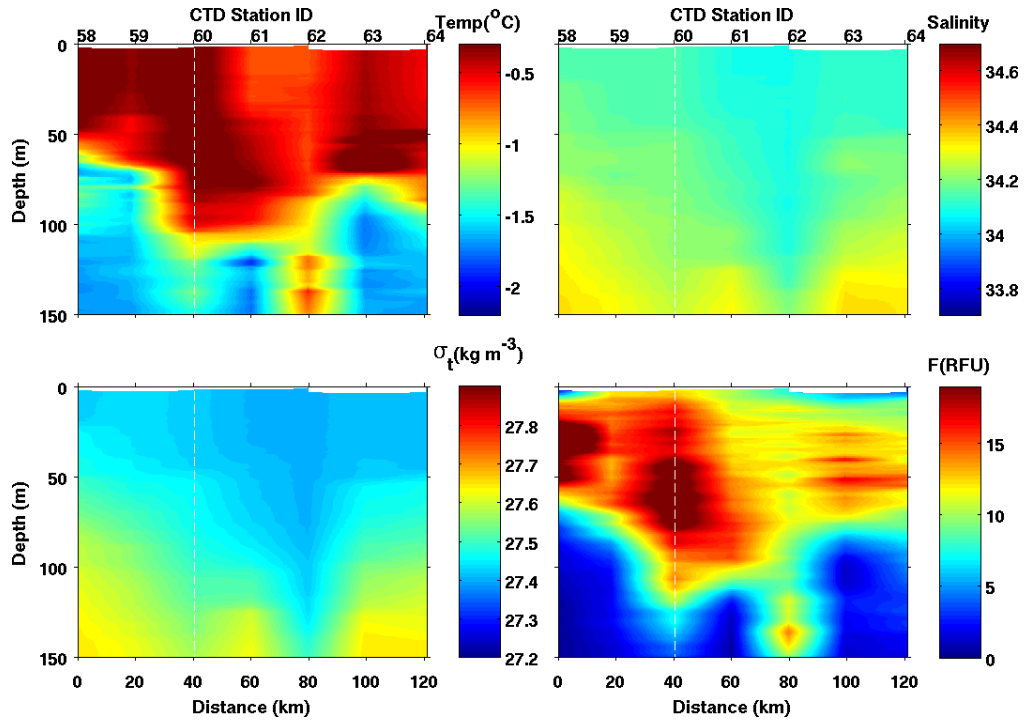
826

827   Fig. 5. Temperature, salinity, σ_t and fluorescence (F) observations for RIS CTD casts (see

828   Fig. 3 for station positions). Fluorescence is in relative fluorescence units, or RFU. Note

829   this relative scale is not the same as that for the VPR observations presented in Fig. 4.

830   The white dashed line indicates the station where the transect orientations shift from
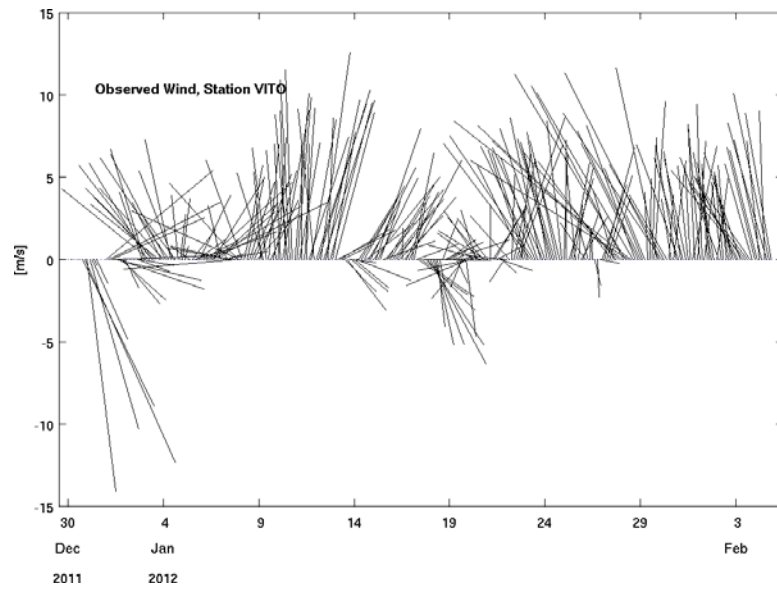
831   north-south to east-west.

832

833

834

835

Fig. 6. Cross-shelf view of ice shelf configuration and model grid. The grids are decimated such that each cell represents 5 by 4 grid points. Insets show zoomed-in views of the temperature and salinity profiles in the initial condition on the upper part of the ice shelf (blue rectangle).
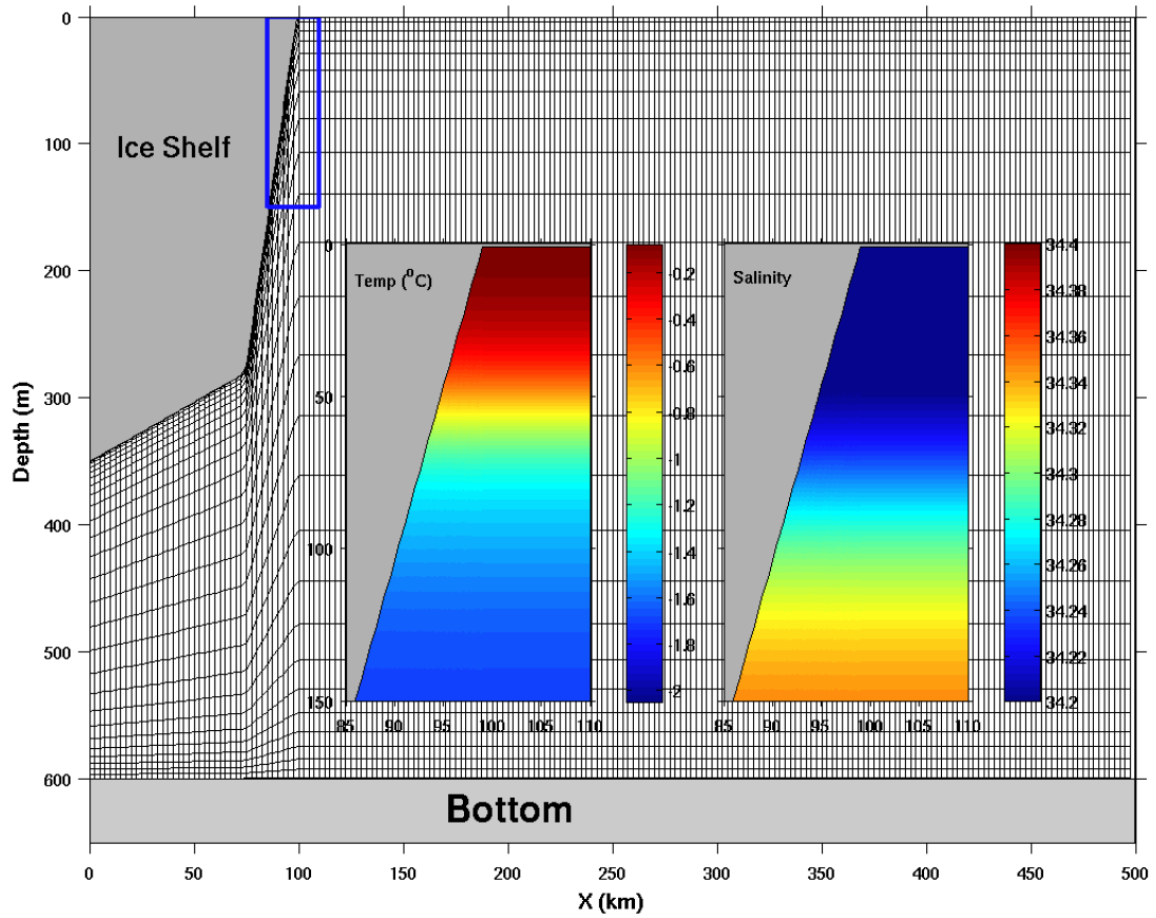
836
837
838
839
840
841
842
843
844
845

Fig. 7. 3-hourly 10-meter wind record from meteorological station VITO (see Fig. 1 for station location).
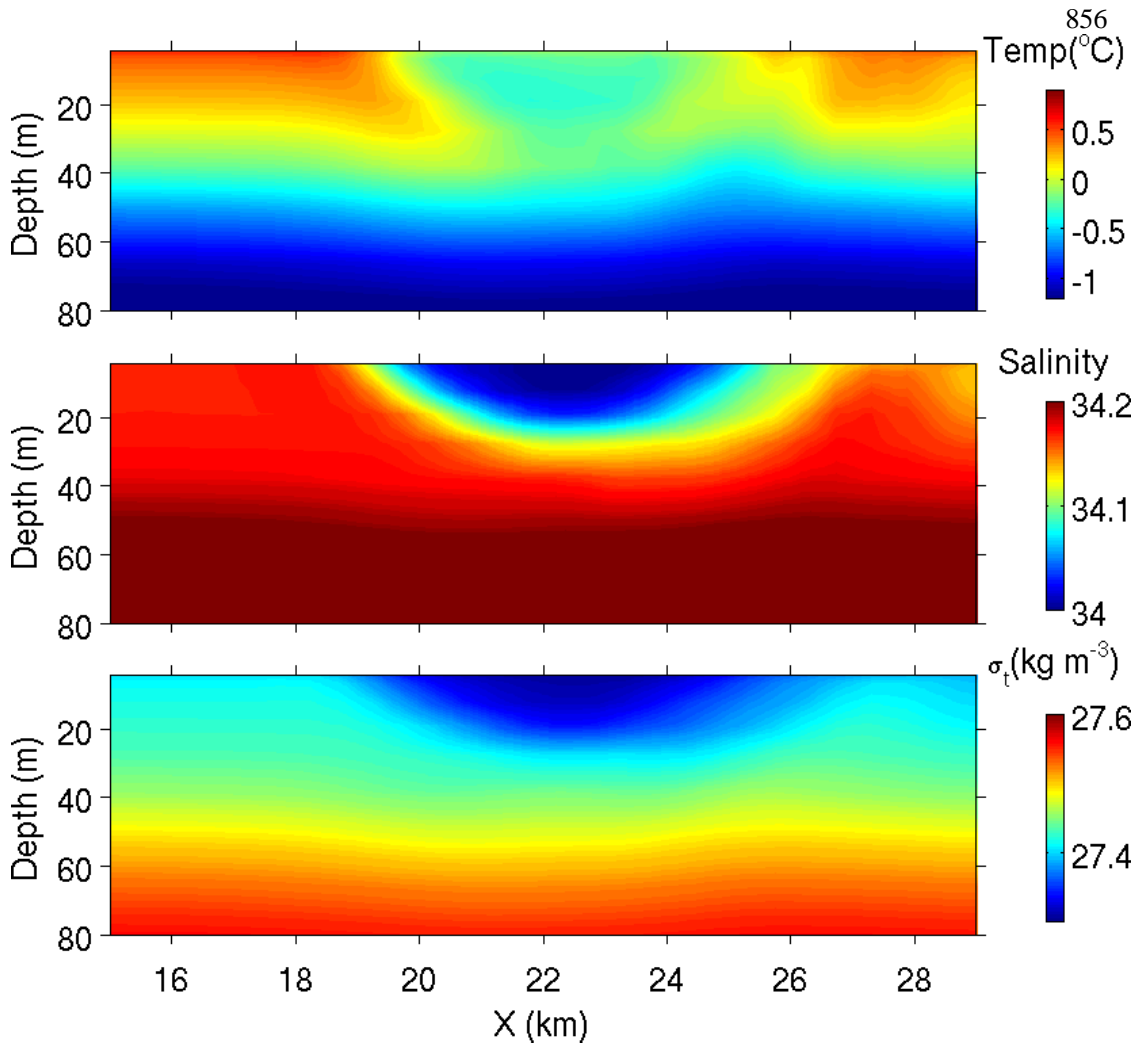
849

Fig. 8. Snapshots of surface temperature and salinity (surface velocity vectors overlaid) at model day 25 listed in Table 1: (a, b) SIS+BM+WIND; (c, d) IIS+BM+WIND; (e, f) IIS+BM. The magenta line in panels c and d indicates the location of a cross-eddy transect shown in Fig. 9.
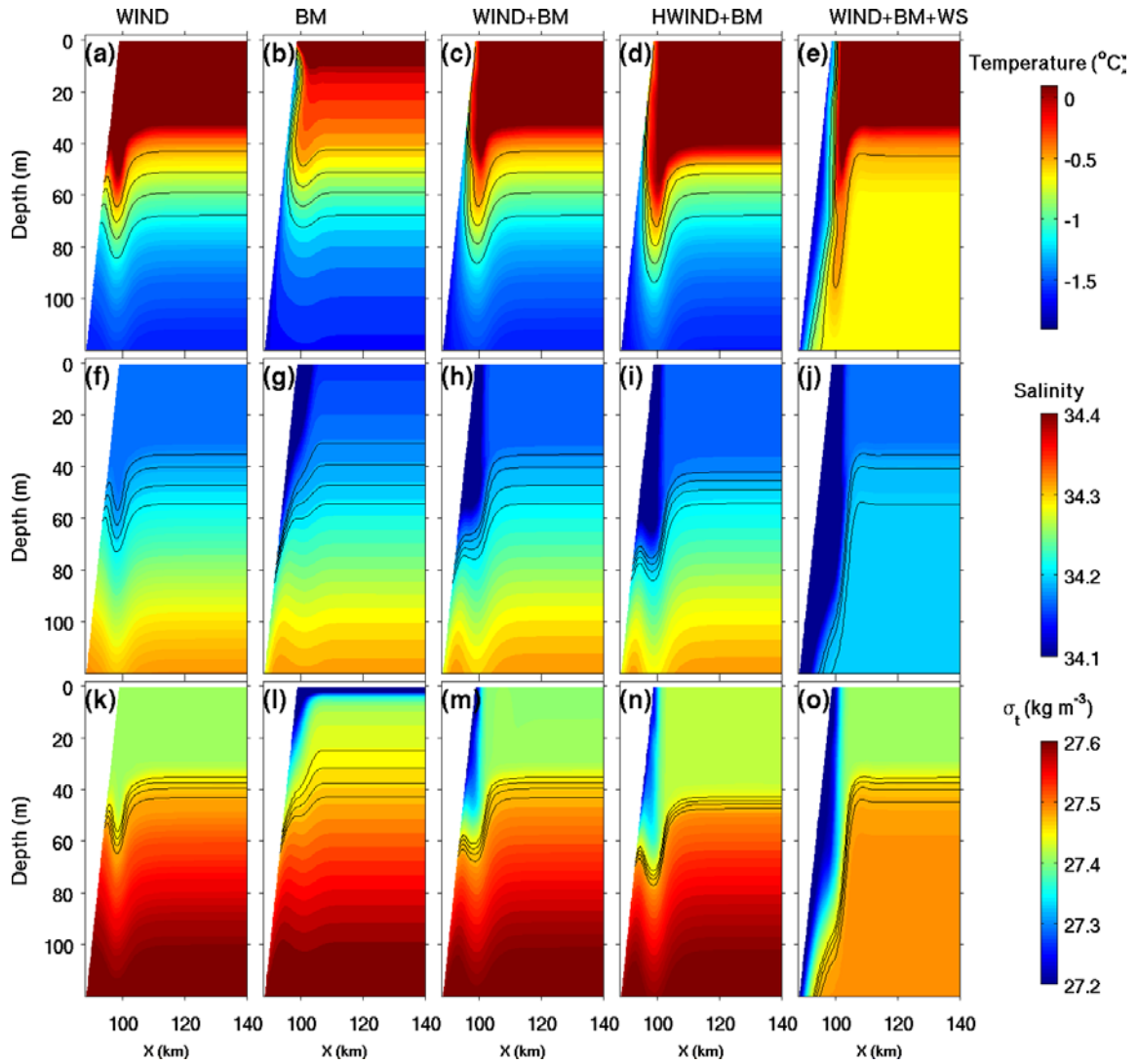
854

Fig. 9. Vertical transect of temperature, salinity and σ_t for the cross-eddy transect indicated in Fig. 8.

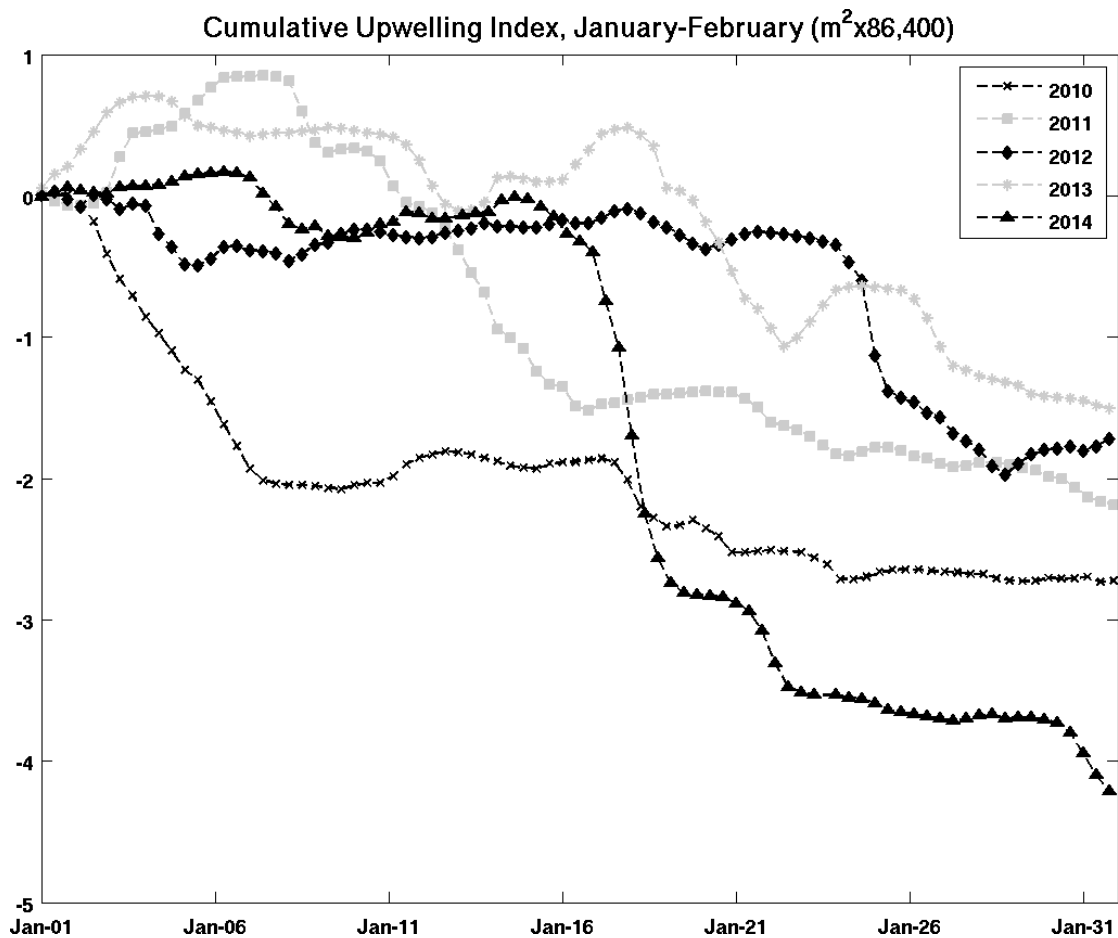Fig. 10. Snapshots of temperature, salinity and σ_t on model day 29.5 for 2-D experiments listed in Table 2: (a, f, k) WIND; (b, g, l) BM; (c, h, m) WIND+BM; (d, i, n) 2D HWIND+BM; (e, j, o) 2D WIND+BM+WS. Solid contours highlight key isotherms (-1.1 to -0.5 °C at intervals of 0.2 °C), isohalines (34.18 to 34.21 at intervals of 0.01), and isopycnals (27.45 to 27.48 kg m^{-3} at intervals of 0.01 kg m^{-3}).

.

896
897
898
899

Fig. 11. Cumulative Upwelling Index (CUI) for the Januaries in 2010-2014.

900
901
902
903
904